RSC Advances

ROYAL SOCIETY
OF **CHEMISTRY**

www.rsc.org/advances

Effect of crystallographic orientation on the tribological behaviour of electrodeposited Zn coatings

K. R. Sriraman[*], P. Manimunda[*], R. R. Chromik[1] & S. Yue

Department of Mining & Materials Engineering
McGill University, Montreal, Qc, Canada H3A 2B2

Abstract

Electrodeposited Zn coatings are currently being used in automotive and aerospace industries for cathodic protection of high strength steel fasteners and components. These coatings are polycrystalline and exhibit preferred orientation depending on the deposition parameters and undergo varying contact stress during their service. This necessitates understanding the role of crystallographic orientation of the coatings on their friction and wear behaviour. In this study, Zn coatings were electrodeposited on low carbon steel substrates with different orientations by modifying plating conditions. A reciprocating pin on disc tribometer with a steel counter sphere under a constant normal load, was utilized to understand the role of orientation of the coating on coefficient of friction (COF), and sliding behaviour of the coatings. Ex-situ analysis of the tribo/ transfer films was performed with X-ray diffraction, nano-indentation, Raman spectroscopy, electron microscopy and nano-indentation techniques. The crystallographic orientation of the coating – tribo/transfer film was correlated to the tribological behaviour, strain hardening and third body formation during contact conditions.

* *denotes equal contribution as first authors*

1 *corresponding author –* richard.chromik@mcgill.ca

Introduction

Electrodeposition of zinc has been widely used for the past two centuries for galvanic protection of steel from corrosion. Various bath chemistries of zinc have been utilized to generate coatings, namely alkaline cyanide baths, acid chloride baths and non-cyanide alkaline bath. These bath chemistries gave rise to field oriented whisker type coatings, field oriented coherent type deposits with grain sizes constant throughout the deposit thickness and unoriented dispersed type crystals with fine distributed grain sizes[1]. Rack and barrel plating processes utilize the alkaline non-cyanide baths and the acid chloride baths, while the cyanide bath became obsolete due to environmental regulations due to toxicity[1]. While plating large and intricate components, in the outer cylinder of the landing gears of an aircraft, by rack plating processes, if there are lack of conforming electrodes, there could be preferred orientation effects on the coating in the recesses. This could lead to anisotropy in the coating properties of wear and corrosion resistance. The texture of the deposit depends on plating conditions, bath chemistry current density, pH of the plating bath, additives added, substrate grain orientation and the nature of the substrate surface finish. Tomov et al[2] investigated the texture evolution in Zn deposits from zinc chloride based plating bath. The texture of the coatings depended on the additive inhibitors added on the bath. The bath without inhibitors produced random orientations on the Zn coatings while the baths with additives resulted in coatings with strong (110) and (100) orientations. The crystallographic orientations of the coatings produced from the plating baths were also dependent on the orientations of the substrates which were Cu and Ni in this case [2] . Mouanga et al [3, 4] reported that in a chloride based plating bath, additives coumerin and thiourea changed the deposit orientation from (112) to a strong (110). They also reported that additives guandin and urea had no effect in crystallographic reorientation of the deposits[4]. Raeissi et al, [5-8] investigated texture evolution in zinc based coatings produced from a zinc sulphate based bath, while evaluating all electrodeposition parameters. Their observations are as follows. The texture of zinc electrodeposits also greatly depends on nucleation and growth mechanism. Strong γ fiber on the cold rolled annealed steel substrate promotes evolution of texture components without fiber[5]. Higher overvoltage on the electrode surface, which was achieved by increasing the current density, increased the basal plane intensity [6]. Finer substrate finish also promoted mixed orientation on the coating, i.e. basal fiber along with non-fiber pyramidal plane orientations (115)

or (116) [6]. Mechanically polished surface yielded weak (115) and (116) fiber texture and the basal plane texture completely disappeared. Some pyramidal component of (101), (102) planes was observed to a lower extent [8].

Zinc coatings are used for corrosion protection on threaded fasteners in different applications[9]. The aerospace industry has been using cadmium over several decades for galvanic protection of steel. As cadmium is toxic, use of cadmium has been restricted, which led to development of various alternatives which are Zn based. The leading candidate among the alternatives is Zn-Ni. Even though there has been a lot of documented research on the properties of Zn-Ni alloy[10-12] there is a lack of literature on the orientation effects on the properties of Zn based coatings.   In recent times Li et al studied the deposition parameters[13], corrosion behaviour[14] and tribological behaviours[15] of nanocrystalline Zn coatings by pulsed electrodeposition methods.   Even though Li et al[15] studied the wear behaviour of Zn by electrodeposition the focus of their work was mainly the effect of grain refinement on the mechanical properties and wear behaviour rather than the crystallographic orientations.   Other than Zn-Ni alloys there is also considerable interest shown on the development of Zn-Co and Zn-Fe deposits as potential Cd replacement [16, 17]. In order to evaluate the Zn based alloy coatings as Cd replacement, a thorough understanding is required of the properties of baseline coating, which is the Zn metal in this case. Zn is a soft metal and it does not exhibit significant wear resistance compared to harder coatings like electroless nickel.   While being applied on a threaded fastener, for a softer coating the tribological behaviour, transfer tribo film rheology[10] becomes important during torquing and removal / reinstallation of the fastener. The platting industry uses acid chloride based plating solution for majority of applications rather than the sulphate based plating bath, owing to easy bath handling and disposal of chloride ions as opposed to sulphate ions, but there is no fundamental understanding of why Zn with different orientations exhibit different behaviour in industrial applications.

The current work investigates the role of coating texture and orientation on the tribology of the electrodeposited Zn coatings obtained from two different bath chemistry. The friction and wear behaviour of the coatings was correlated with tribo-transfer film evolution using X-ray diffraction, electron microscopy, indentation and spectrochemical analyses.

Experimental Methods

Coating deposition

Two different plating baths were chosen, a $ZnCl_2$ based plating bath and a $ZnSO_4$ based bath in order to obtain Zn coatings with different orientations / texture. A general purpose low carbon steel sheet SAE 1008 grade steel was used as a substrate material. The substrate was prepared with SiC abrasive grinding paper with 600, 800 grit finishes and then fine polished with 0.05µm colloidal SiO_2 suspension.   The substrate was then acid pickled in 10% HCl solution for the chloride bath and 10 % H_2SO_4 solution in case of the sulphate plating bath, before electrodeposition of the coating. The bath chemistry and plating parameters are given in Table 1. An EG&G PAR – Model 363 potentiostat / Galvanostat was utilized for electrodeposition of the coating on a galvanostatic mode with two electrode set up. The deposition was carried out to a constant coating thickness of 20-25µm in a glass beaker with pure metallic Zn as a counter electrode.

Table 1. Bath chemistry and plating parameters for electrodeposition of Zn

Chloride bath		Sulfate bath	
Chemistry	Concentration (g/L)	Chemistry	Concentration (g/L)
$ZnCl_2$	60	$ZnSO_4$	620
KCl	250	Na_2SO_4	72
H_3BO_3	25	H_2SO_4	<10
HCl	<1		
Other plating parameters			
Chloride bath		Sulfate bath	
Current density (mA/cm^2)	5	10	
pH	4.2	2	
Plating time (hours)	3	1.5	
Coating thickness (µm)	20-25	20-25	

Tribology tests

Wear tests were performed with a reciprocating motion using a custom-built reciprocating ball on disc tribometer [18, 19]. A hardened stainless steel ball of AISI 440C grade (6.35mm diameter) was the slider against the coating with 3.98 N force and the initial maximum Hertzian contact pressure was 750 MPa. The tests were conducted at 14 mm/S sliding velocity and the track length was 20 mm. The maximum sliding cycle was 2000 cycles, resulting a total sliding distance of 46.54 m. The friction was monitored throughout each test using a piezoelectric transducer, which samples lateral forces at the rate of 2000 Hz. An average friction coefficient was calculated for each friction cycle, where the central region of each track was used in the calculation. Data near the turnaround points ~ 1% of the track length, was omitted from this calculation. To generate the wear data at different intervals of sliding cycle, separate 20 mm length tracks were obtained at 10, 50, 100, 200, 500, 850, 1200 and 2000 cycles. There tracks were used for ex-situ mechanical and texture analysis. The present work also aimed at understanding the chemical changes associated with sliding. For chemical analysis, it is mandatory to generate wear tracks at similar laboratory conditions (humidity and temperature). A stripe test was performed where in a single test, tracks corresponding to 10, 75, 200, 500, 850 and 2000 sliding cycles were generated and used for chemical analysis. A stripe test is a wear test where an initial track length of 20 mm was reduced by 2 mm at a time after a certain number of cycles have passed [20]. In other words, one single wear track will have sections corresponding to different sliding distances. This method facilitates rapid estimation of physio-chemical changes during a wear test and helps to identify the areas of interest that may need detailed examination[20].

Characterization techniques

Wear track morphology, crystallography and elemental and chemical nature were studied using scanning electron microscopy (SEM), X-ray diffraction (XRD) and Raman spectroscopy. An FEI Inspect F50 field emission gun SEM coupled with energy dispersive spectroscopy (EDS) was utilized to observe the surface and cross sectional morphologies, tribo/transfer films, and wear track morphologies of the coatings. Coating thickness was estimated with both the weight gain

method and also by microscopy of the cross sections. The coating and tribo film texture were measured using a Bruker discover D8 – HISTAR 2D, area detector diffractometer with Co-Kα radiation with a 0.8 mm collimated X-ray beam in a standard ɵ -2ɵ configuration. The pole figures were measured in the goniometer by simultaneously measuring all the three reflections of Zn (002), (100) and (101) in one measuring frame and then integrated using Bruker Multex software. These raw pole figures were subsequently utilized for calculating the orientation distribution function (ODF) and were normalized based on the ODF with the TexTools software. The chemical composition of the wear track as well as debris were analysed using an InVia Raman microscope (Renishaw, UK). The excitation source was 514.5 nm Ar+ laser. During spectral acquisition to avoid sample damage, neutral density filters were used to decrease the laser power to 5 mW. The Raman scattered light was collected in a backscattering geometry using Leica 50x objective lens. Raman scattered light was dispersed using a grating of 1800 lines/mm. The resolution of the spectrometer was 1 cm^{-1}. The spectral acquisition time was fixed to 10 seconds.

The hardness, H and reduced modulus, E^{*} of the coatings, as well as the transfer film, were determined using an instrumented nanoindentation technique (Triboindentor, Hysitron, USA). The force and displacement sensitivity of the instrument were less than 30 nN and 0.2 nm respectively. A diamond Berkovich tip (tip radius ~100 nm) was used for the indentation test. Indentation experiments were done in load control mode with peak loads varying from 40 µN to 1 mN. The load displacement curves obtained were fitted using the Oliver-Pharr method [21, 22].

Results and discussions

Coating Characteristics

The surface morphologies of the coatings deposited from two different plating solutions are given in Fig. 1. The morphology of Zn coating obtained from the $ZnCl_2$ bath depicts most commonly observed cauliflower type morphology [23]. The platelet size was ranging from 2 – 5 µm. The Zn coatings obtained from the sulphate bath comprised of clusters of individual hexagonal platelets which are typical of Zn coatings deposited from mechanically finished substrate surfaces [8].
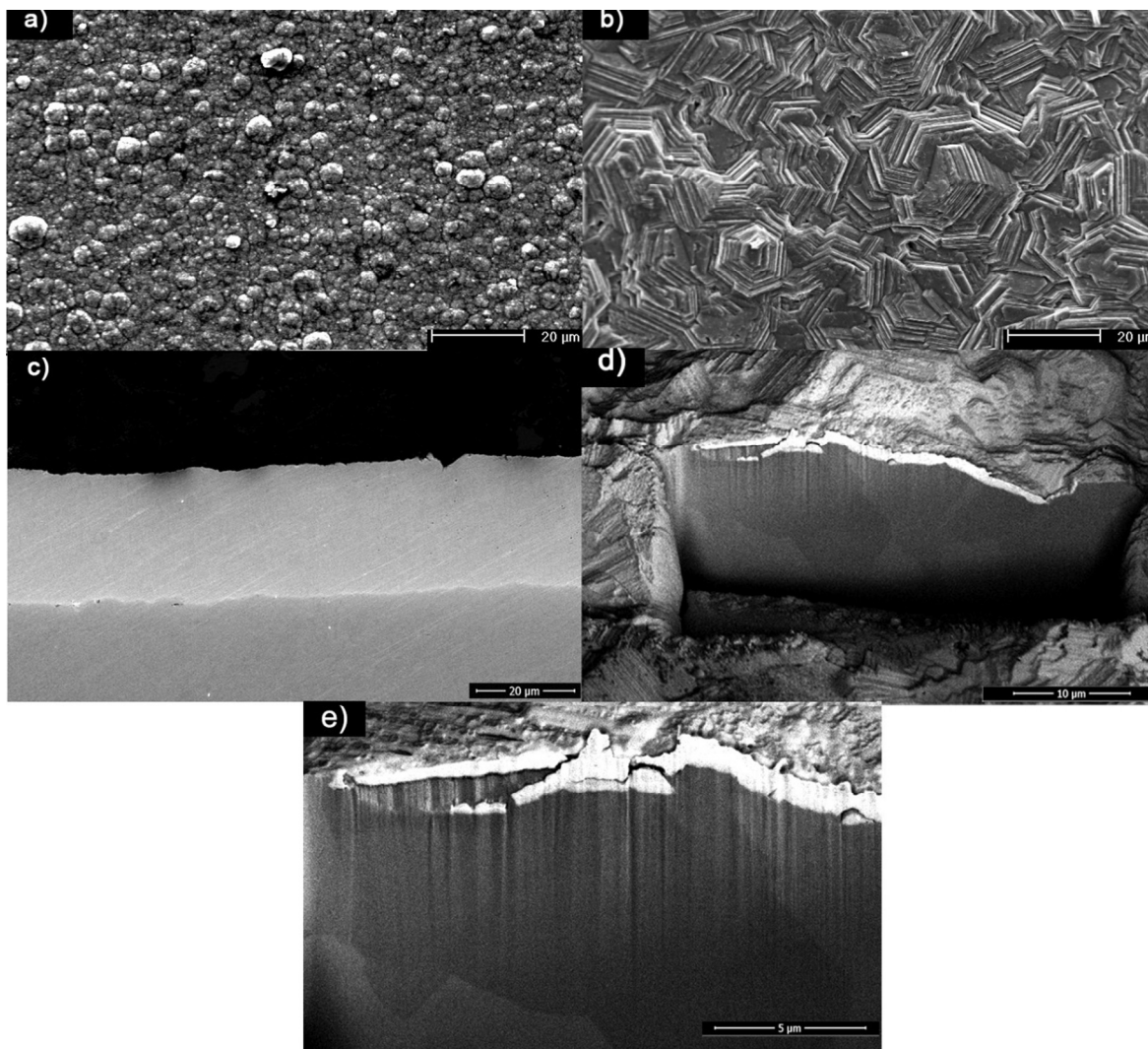
Fig 1. (a) Surface morphology of Zn from chloride bath (b) Surface morphology of Zn form sulphate bath (c) metallographic cross sectional morphology of Zn from chloride bath (d) & (e) FIB trench cut cross section of Zn from sulphate bath

The cross sectional morphologies of the coatings are shown in Fig 1 (c) -(e). The coatings obtained from chloride bath showed a uniform dense interface owing to the spherical morphology of the coating, which enabled close packing of the platelets. The coatings obtained from the sulphate bath were hexagonal platelets bunched over each other and hence the surface coverage was not uniform resulting in higher surface roughness. Preparation of cross sections of these coatings by metallographic methods led to artefacts due to the platelets pulling out during

polishing thus, a focused ion beam (FIB) rectangular trench (15 µm in depth) was cut from surface. The observed coating cross section was uniform with well-defined grains along the thickness.
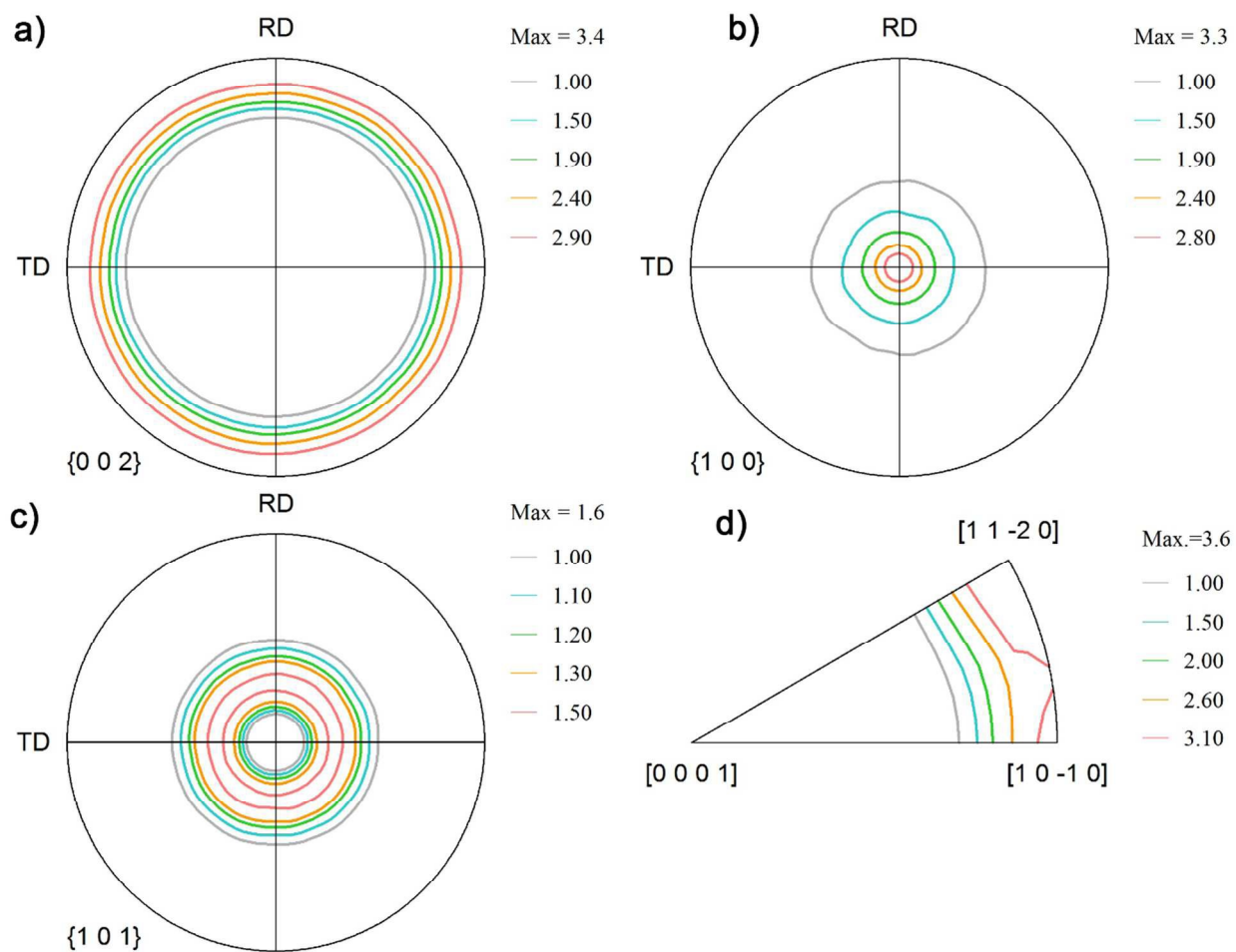
Fig 2. Pole figure notation of the orientations on the coatings obtained from chloride plating bath a. (002) b. (100) c. (101) d. Inverse pole figures.

The pole figure showing the distribution of crystallographic orientations for the Zn coatings obtained from the chloride bath are shown in Fig. 2. These coatings exhibit a stronger (100) fiber texture Fig 2(b), i.e. the (100) planes are oriented in the normal direction (ND) which is perpendicular the frame of reference or in the 'Z' direction. The other two reference directions are the rolling direction (RD) and the transverse direction (TD). From Fig 2 (a) and (c) a weak

(101) fiber and absence of basal fiber was observed.[2]. The inverse pole figure in Fig 2(d) showed that this coating also exhibits a weak pyramidal plane (110) and a strong prism plane orientation (100). The presence of (100) and (110) textures on the coatings deposited from the chloride bath was owing to lower overvoltage, and also the presence of zinc hydroxide ions near the cathode surface which cause an auto inhibitor effect in the absence of any additives[2]. This coating would be referred as Zn $_{(100)}$ for the sake of convenience in the article henceforth.
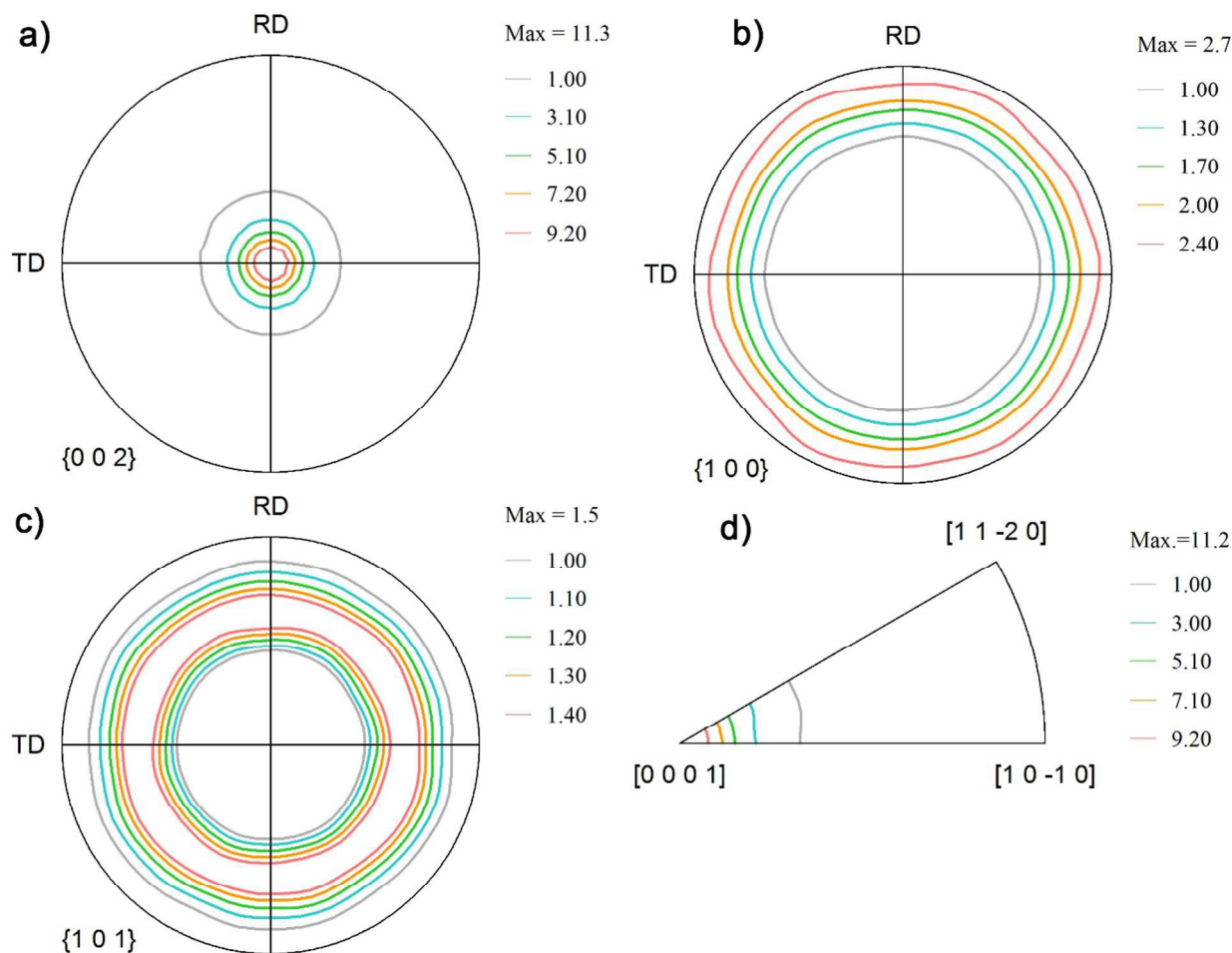
Fig 3. Pole figure notation of the orientations on the coatings obtained from chloride plating bath a. (002) b. (100) c. (101) d. Inverse pole figures.

The pole figure of Zn coatings, which are deposited from the sulphate bath, are shown in Fig. 3. This coating shows a very strong basal plane fiber i.e. all basal planes oriented in the normal direction of the reference frame. The inverse pole figure in Fig. 3 (d) also shows absence of pyramidal or prismatic plane reflections and only basal plane intensities populating the map.

The pole figure observations from both the coatings corroborate the observations in the surface morphology. The Zn coatings from the chloride bath has randomly distributed spheroidal plates while in the coatings obtained from sulphate bath, the basal plates are stacked vertically i.e. aligning towards plane normal. Coatings from the sulphate bath exhibits a strong basal plane orientation owing to higher overvoltage relating to higher current density and faster nucleation of the grains as compared to the chloride bath[6, 7]. This coating would be referred to as Zn $_{(002)}$ for the sake of convenience in this article henceforth.

Mechanical properties of the coating measured using the nanoindentation method is shown in Fig. 4. The roughness (R_a) of the as plated Zn $_{(100)}$ and Zn $_{(002)}$ were 0.7 and 5 μm respectively. Surface roughness was reduced by grinding them a fine 4000 grit SiC paper, and subsequently chemico-mechanically polished in an alcohol based Al_2O_3 suspension (50 nm particle size). Polished coatings with 30-100 nm surface roughness was used for indentation tests.
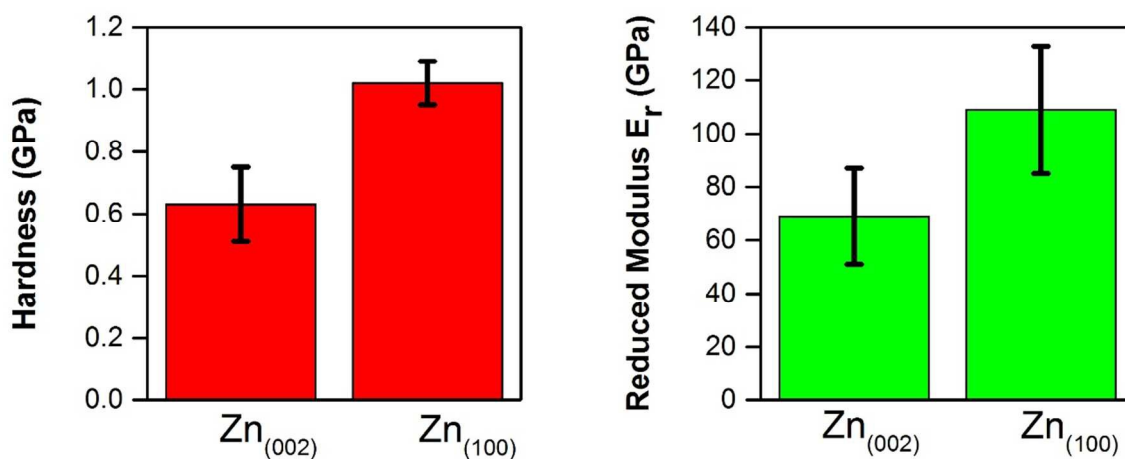
(a)
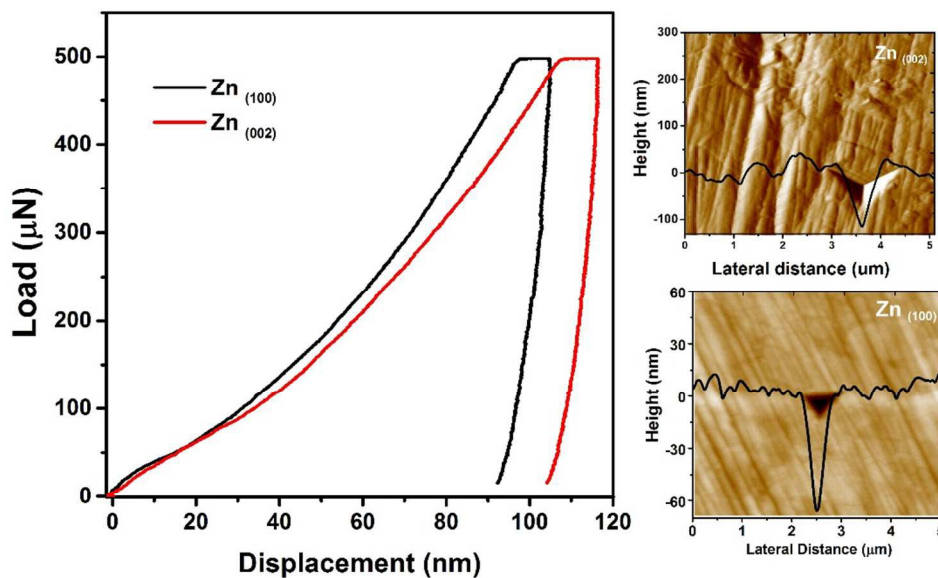
(b)

Fig 4. (a) Hardness and reduced modulus (E_R) of the coatings. (b) Typical load displacement curves and SPM images of the indents

The average hardness for the basal plane orientated coating (sulphate bath, Zn $_{(002)}$) was 0.63 GPa and 1.02 GPa for the prism plane coating (Zn $_{(100)}$). Both coatings showed different measured modulus. Measured modulus for Zn $_{(002)}$ coating was 69 GPa whereas Zn $_{(100)}$ coating had 110 GPa. The measured mechanical property data suggested a strong dependency on coating orientation. For Zn $_{(002)}$ coating, majority of the basal planes were parallel to the substrate. When indentation was done on the basal plane, the larger c/a ratio (1.856)[24] of Zn resulted in lower modulus. In addition to the orientation, the lower compactness (figure 1b) resulted in inferior mechanical properties.

Friction and wear behaviour

The friction force evolution with respect to the number of sliding cycles for the coatings at 750 MPa initial Hertzian contact pressure is shown in Fig. 5a.

(a)   (b)
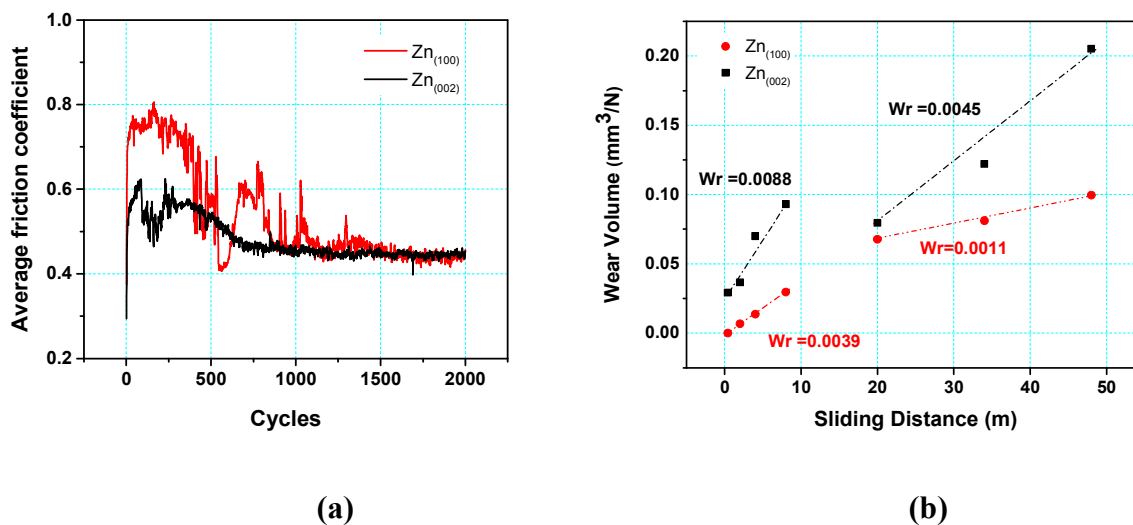
Fig 5. (a) Variation of average friction coefficient versus number of cycles (b) Variation of wear volume versus number of cycles.

The friction traces showed distinct regimes for both the coatings; a prolonged running-in period (up to 500 cycles) followed by an unsteady or reduced friction (500-800 cycles) and a steady state regime (800 -2000 cycles). During running-in period (first 10 cycles) the coefficient of friction (COF) for the Zn $_{(100)}$ coating increased to 0.8 from initial value of 0.3. The friction coefficient then stabilized until 500 cycles and then dropped to 0.4. The COF increased again to 0.6 at 600 cycles and dropped off to 0.4 at 800 cycles and therein stabilized to a value of 0.45 till the end of the wear test. Whereas for Zn $_{(002)}$ coating, the COF increased to a lower value of 0.6 from 0.3 within the initial 10 cycles. A drop in COF was observed at 200 cycles and then again it increased to 0.6 at 250 cycles. The friction coefficient started to slowly decrease from 400 cycles to 750 cycles from 0.6 to 0.45 and therein stabilized to that value till the end of the test.

Fig. 5b shows the variation of wear volume as a function of sliding distance. The wear volume of the Zn $_{(100)}$ coating was lower than that of the Zn $_{(002)}$ coating. The primary reason for the lower wear of the (100) coating was its higher mechanical properties (c.f. Fig 4). Both coatings also exhibited two distinct wear regimes (see Fig. 5b). For less than 10 m of sliding, a higher wear was observed. This was followed by a steady state period with a lower wear for greater than 10 m of sliding. While the wear rates decreased for both coatings after 10 m sliding distance, the

wear and wear rate for the Zn $_{(002)}$ coatings (88 X 10^{-04} mm^3/Nm) was higher than Zn $_{(100)}$ (39 X 10^{-04} mm^3/Nm) coatings.

Ex-situ analyses of wear track and counter body
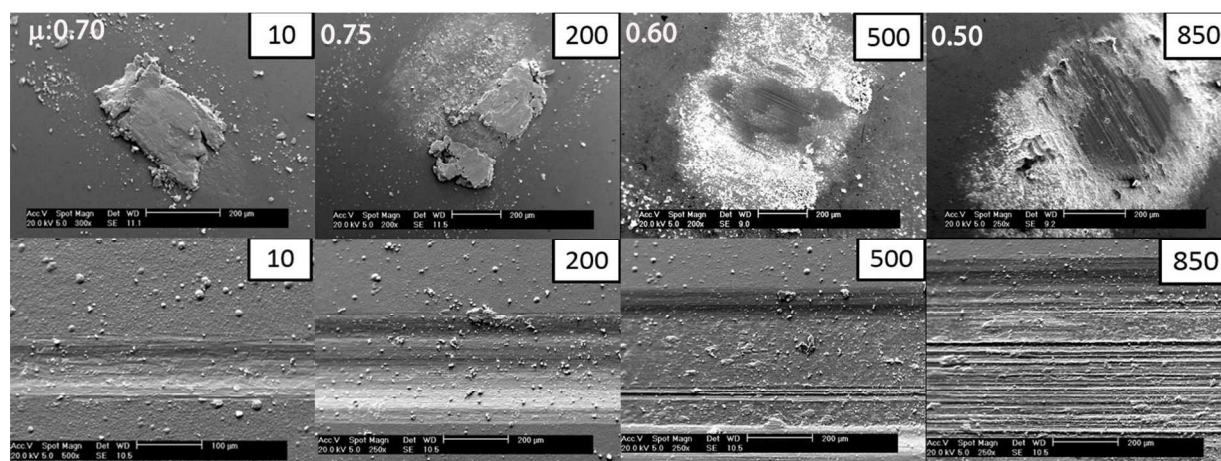
Fig 6. Ex-situ SEM micrographs of the counterface (top) and wear track (bottom) of Zn$_{(100)}$ coatings.

The friction behaviour observed in Fig. 5 can be explained with the help of the ex-situ analyses of the third bodies on the counterface and the surfaces of the worn coatings. The ex-situ SEM analyses of the counterfaces (top) and wear tracks (bottom) of the Zn $_{(100)}$ coating are shown in Fig 6. Adhesive wear dominated the early sliding cycles. The presence of thicker transfer film on the counter body after 10 cycles increased the COF from 0.3 to 0.8. At 200 cycles, a point in the test where the COF was relatively stable at 0.75, the transfer film on the counter surface was still present but started to break apart and some parts spalled off from the surface. On the coating, the wear track widened and there was evidence of scattered wear debris within the track. At 500 cycles the friction momentarily dropped to 0.4 and then increased to 0.6. At this stage most of the transfer film was removed, with some thinner transfer film in the centre and scattered loosely adhering granular white debris on the sides, indicative of oxidational wear. The effective contact area on the counter surface also increased. With increase in sliding cycles the granular materials present at the track re deposited on to the ball surface. This kind of transfer film rheology is well documented through in-situ tribology technique on these kind of coatings elsewhere[11]. At 850 cycles the counter surface is devoid of any transfer film in the centre, with accumulated third bodies on the side accompanied by further increase in the contact area. Detailed chemical

analysis of the debris and transfer films were conducted to understand the wear mechanism, the results are presented in the later sections.
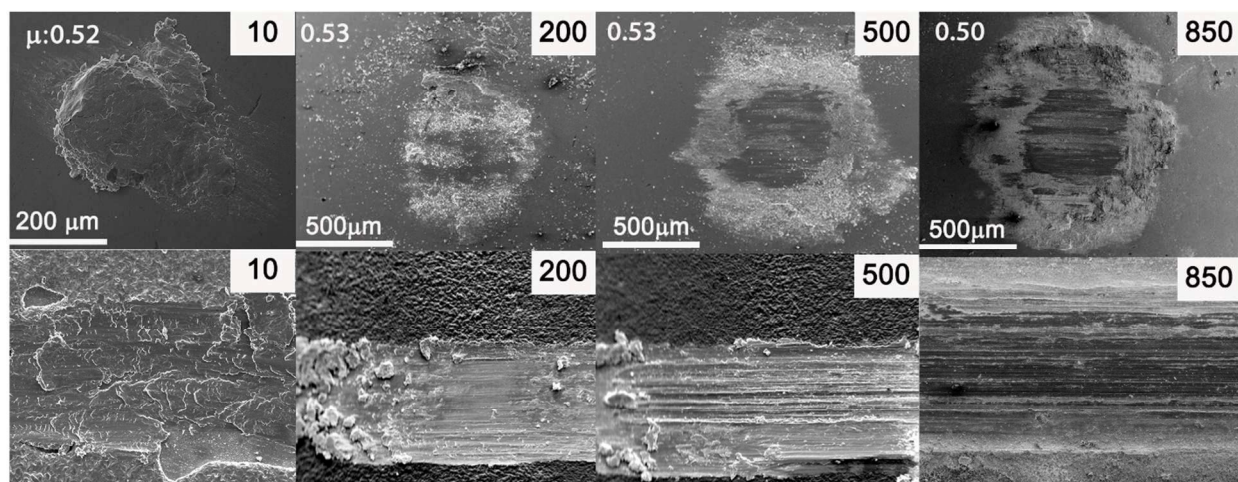
Fig 7 Ex-situ SEM micrographs of the counterface (top) and wear track (bottom) of Zn$_{(002)}$ coatings.

The ex-situ SEM analyses of the Zn $_{(002)}$ coating is shown in Fig 7. In early stages, the formation of a thick transfer film accompanied by a rise in friction was similar to the Zn $_{(100)}$ coating. However, as shown in Fig. 5a, the friction rise was only to 0.52, whereas for the Zn $_{(100)}$ coating it was 0.7. Clear differences are also observed for the ex-situ analysis at cycle 10, where there is formation of a wide wear track and an accompanying wide transfer film on the counter surface. Also, the wear track for Zn $_{(002)}$ exhibited a fish scale type morphology suggestive of adhesive wear. The softer Zn $_{(002)}$ coating showed much more wear in the early cycles compared to the Zn $_{(100)}$ coating (see Fig 5b). In addition to mechanical properties, the dominant factor for wear of this coating was the orientation of the basal plane. For Zn $_{(002)}$ coating, the basal plane was parallel to the sliding direction. In this configuration, lower shear stresses are sufficient to induce the basal cleave and hence larger wear at a lower level of friction. The observed wear rates are in good agreement with previously reported data for electrodeposited Zn on copper substrate[25]. At 200 cycles, the Zn $_{(002)}$ exhibits a loss of transfer material in the counter surface and white granular debris started to appear. At 500 cycles the contact area on the counter surface is increased with compact transfer film on the circumference. At 850 cycles there is very minimal transfer film accumulation on the centre of the contact. The wear track shows formation of a

dark layer with minimal coating adhering to the surface. The composition of this tribo layer will be discussed in detail using spectral analyses.

Crystallographic orientations and mechanical properties of the wear tracks

The orientation of the $Zn_{(100)}$ and $Zn_{(002)}$ wear tracks as a function of sliding cycles are shown in Fig 8. The orientation of the $Zn_{(100)}$ wear track (Fig 8.) remained the same as the unworn coating until 200 cycles. The (100) fiber begins to spread along the rolling direction (sliding direction) at 500 cycles. This shows a transformation in the wear track orientation. The pole figures measured on the wear track after 2000 cycles had a non fiber (100) orientation which is a consequence of Zn on the steel grains which is different from the original coating orientation. This change in orientation is due to extensive plastic deformation during the wear test. On contrary to the (100) planes there was no change observed on the (110) planes during the wear except the planes changed from fiber to non fiber orientations with reduced intensities. The transfer film layer orientation on the $Zn_{(002)}$ (Fig 8) showed a different behaviour compared to the $Zn_{(100)}$ coatings. The change in basal fiber to non fiber orientations occurred as quickly as 100 cycles. As the wear tests progressed to 200 cycles, the non fiber orientation of Zn basal planes were characterized by appearance of two maximums in the pole figure maximums. Beyond 500 cycles the coating orientation was mixed fiber and non fiber, this could be due to drastic thickness reduction and loss of coating volume and most of the tribo layers left on the wear track were mixed oxides. The chemical nature of the tribofilm is discussed in the later section.
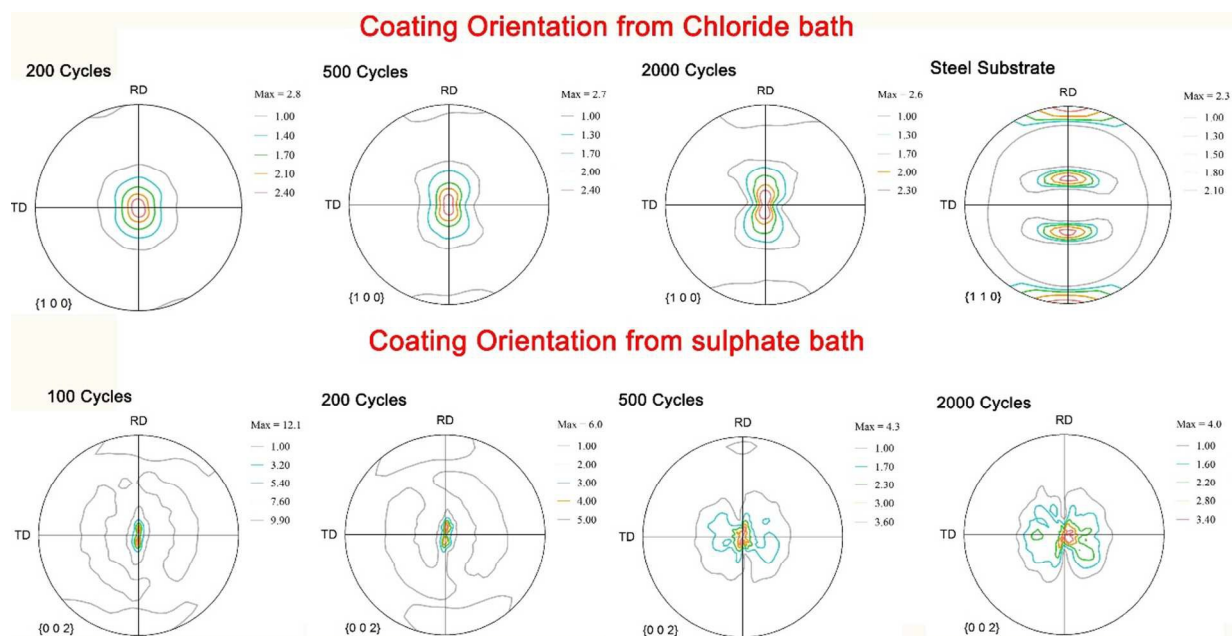
Fig 8. Coating orientations on the track after wear test

Electrodeposited Zn $_{(100)}$ and Zn $_{(002)}$ coatings showed different run-in behaviour. Up to 450 cycles, the Zn $_{(100)}$ coating showed higher friction. The mechanical properties of the wear tracks generated at different sliding cycles were studied by performing nanoindentation at different locations on the wear tracks. Fig. 9a and 9b compares the wear track hardness and modulus variation as a function of sliding cycles for Zn $_{(100)}$ and Zn $_{(002)}$ coatings respectively. Up to 50 cycles there was no significant increase in hardness for Zn $_{(100)}$ wear track and the values are comparable to that of the as deposited coating (see Fig 4) but at 100 cycles the hardness increased from 1.2 to 1.8 GPa. After 100 cycles till 500 cycles the hardness begins to drop to a value similar to that of the unworn coating. On the other hand, Zn $_{(002)}$, wear tracks did not show significant increase in hardness. Also at 500 cycles, influence of the substrate was observed on the measured hardness. From ex-situ analyses (Fig 7) it is evident that most of the Zn coating was worn and steel on steel contact started to dominate after 500 cycles.

The observed increase in hardness for Zn $_{(100)}$ coating during the initial 100 cycles were due to sliding induced strain hardening. At early stages of sliding Zn $_{(100)}$ tracks had elongated patches. A cyclic indentation was performed on elongated patches (Fig. 10) as well as wear track to check indentation induced strain hardening. Fig. 10 shows the load displacement curve obtained from

cyclic indent. The deformed patches showed higher hardness when compared to undeformed wear track region. No significant increase in hardness was observed due to cyclic loading.

(a)　　　　　　　　　　　　　　　　　　　　　　(b)
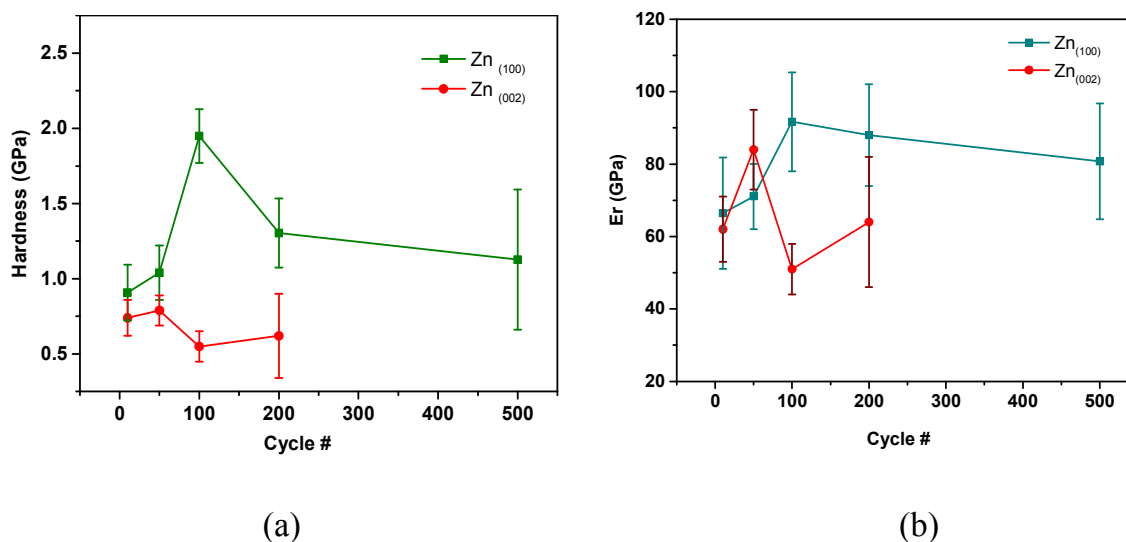
Fig 9. Mechanical properties on the wear track with respect to number of cycles (a) hardness versus cycle number (b) Reduced modulus versus cycle number

For Zn $_{(100)}$ the C- axis is parallel to the sliding direction. It is a very well established phenomenon for zinc, the deformation in C-axis leads to strain hardening. The primary reason for hardening is the formation of dislocation dipoles arising during the intersection of dislocations travelling in any one of the $(11\bar{2}2)$ pyramidal planes.[26] During early stages (10 cycles) of sliding only few patches on the wear track, which are elongated showed higher hardness. Figure 10 shows load displacement curves generated from a partial unloading indentation experiment performed on two regions on the wear track. The SEM micrograph of the indent is also shown in Figure 10. Indentation performed on the elongated patch showed higher hardness (1.8 GPa) at depths <30 nm, and with increase in contact depth the hardness decreased to a value similar to that of the as deposited coating (~1 GPa). Whereas indentation performed on the adjacent track region showed no changes in hardness value with contact depth. From 10 to 100 the contact conditions remained the same and the counter ball surface had a thicker transfer film (see figure 6). Above 200 cycles transfer film started to break and removal of strain

hardened layer decreased the wear track hardness from 1.8 to 1.2 GPa. At 500 cycles, the presence of oxides and the rough wear track produced larger scattering.
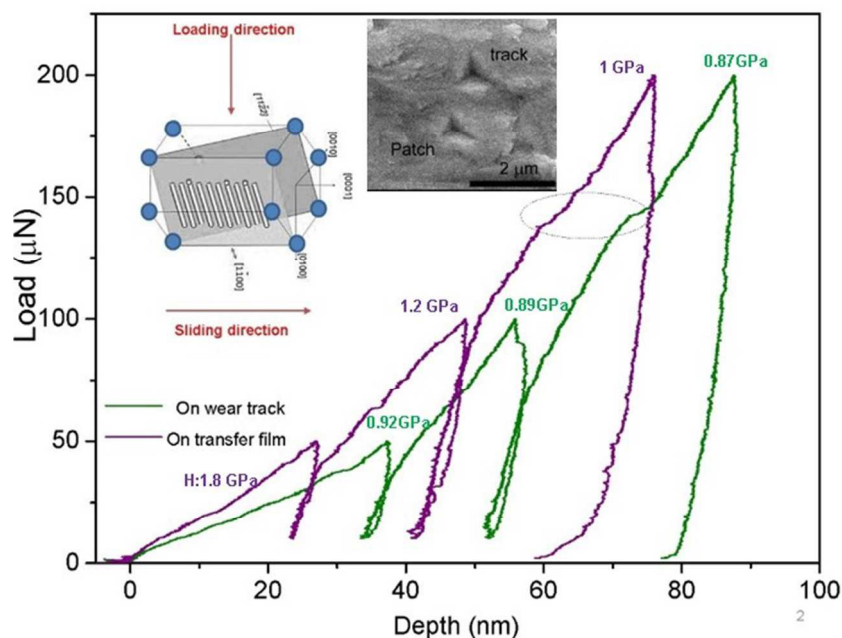
Fig 10. Load displacement curve and corresponding SEM micrograph of the indents obtained from the cyclic indentation on two regions of the wear track of Zn $_{(100)}$ coating.

Chemical analysis of the wear track

Energy dispersive X-ray spectroscopy (EDS) analysis was carried out on the wear track and transfer films (ball surface). For both Zn $_{(100)}$ and Zn $_{(002)}$ coatings at higher sliding cycles (> 100), traces of oxide was detected on ball, wear track (not shown) surfaces. In Fig 11 a, representative SEM micrographs of the third bodies (from Zn $_{(100)}$) and in Fig 11 b, corresponding EDS spectra are shown. At cycles below 50, the debris was predominantly Zn.
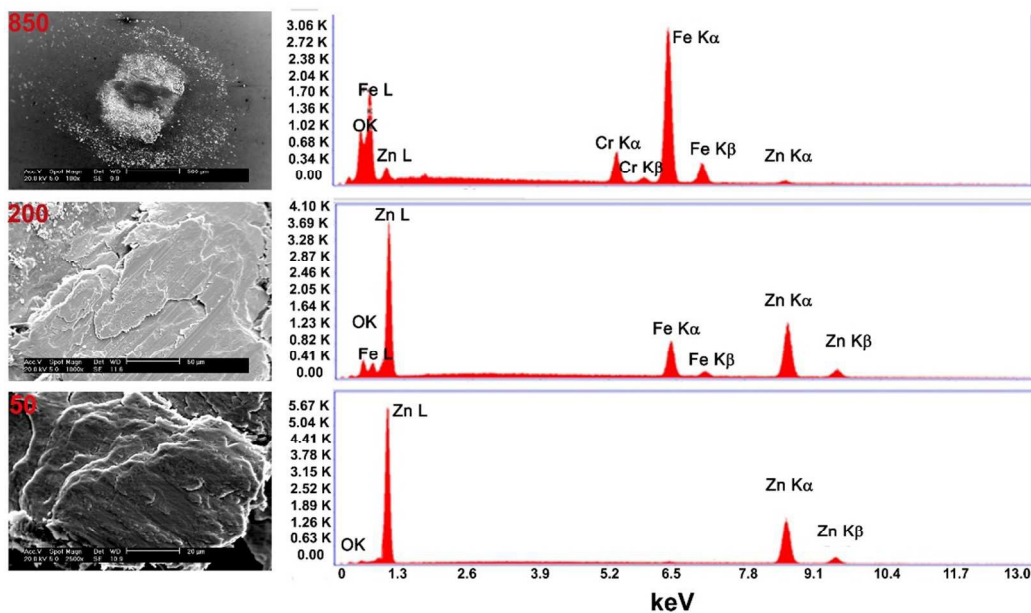
(a)   (b)

Fig 11. a) Representative SEM micrograph of the transfer film on ball surface for Zn (100) b) EDS spectra showing the presence of oxide.

At higher cycles, along with oxygen both iron and zinc peaks were detected. It was difficult to determine whether the oxides formed are zinc, iron or a mixture of both. Previously the study by Li *et al* also showed the transition from adhesive wear to oxidative wear in electrodeposited Zinc coatings[15]. In order understand the chemical process involved during the transition from adhesive to oxidative wear, the transfer films and the wear tracks were analysed using Raman spectroscopy. The Raman spectra recorded from the wear track and ball surfaces for both the coatings are shown in Fig. 12 and 13 respectively.
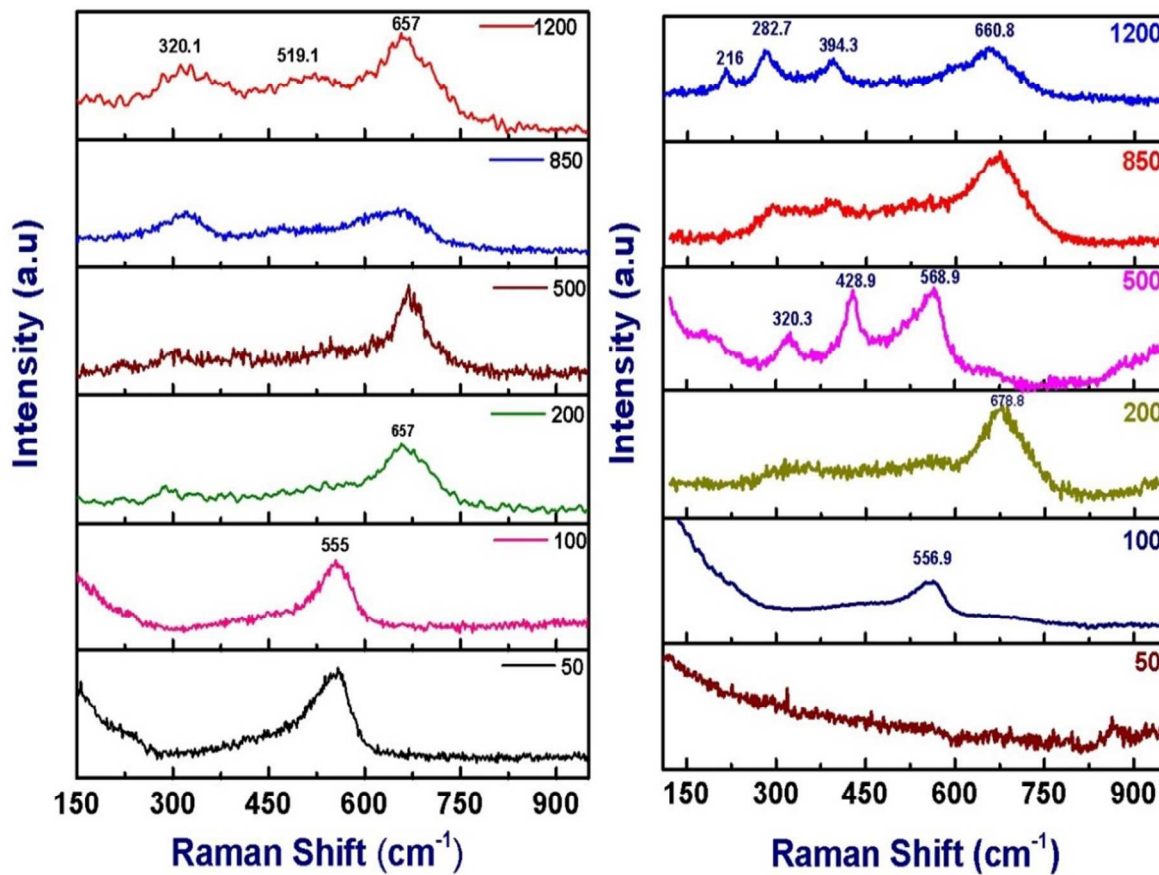
(a)

(b)
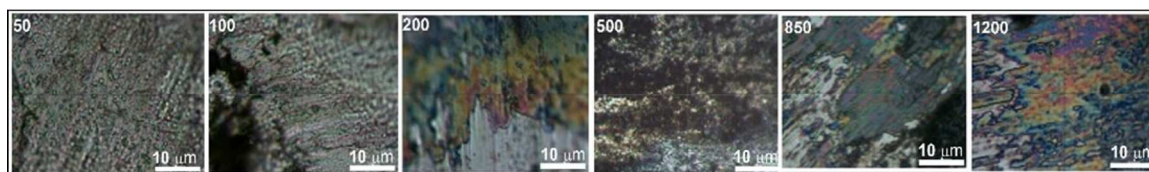
(c)

Fig 12. Raman spectra from the Zn $_{(100)}$ a) from the wear track surface b) from ball surface c) Optical images of the transfer film.
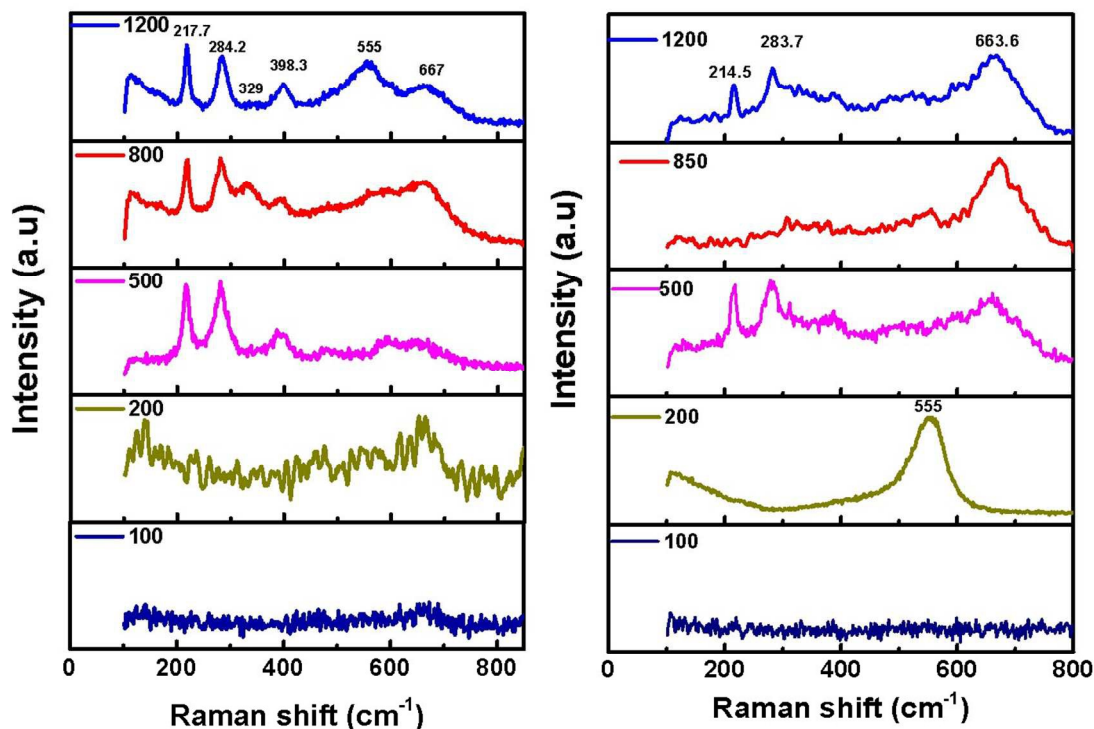
Fig 13. Raman spectra from the wear track Zn $_{(002)}$ a) from the wear track surface b) from ball surface.

In $Zn_{(100)}$ coating up to 100 cycles on wear track and counter face, only one noticeable peak was observed at 555 cm^{-1} (Fig. 13). From the EDS analysis it was confirmed that, the composition of the debris at lower sliding cycles was rich in Zn and the most probable candidate at this stage was ZnO. The 555 cm^{-1} peak could be attributed to A_1 longitudinal optical (LO) phonon mode of Wurtzite[27, 28]. In this study we did not observe peaks corresponding to E_2 (low & high), A_1 transverse optical (TO), E_1 (TO) and E_1 (LO) phonon modes. Since the Zn coatings had a strong texture, an ordered oxide film can be expected. For ordered ZnO films, in back scattered Raman geometry, only A_1 (LO) and E_2 modes can be expected[27], At 200 cycles, a single peak is observed at 657 cm^{-1} corresponding to iron oxide and zinc oxide mixture[29, 30]. At 500 cycles wear track had mixed oxide while the debris showed stronger zinc oxide bands. At higher cycles (above 500) iron oxide dominated in composition. For Zn $_{(002)}$ coatings (Fig.14), ordered zinc oxide was detected only at 200 cycles. Wear tracks obtained at 500 cycles and above showed stronger iron oxide peaks[31-33].

(a) **(b)**
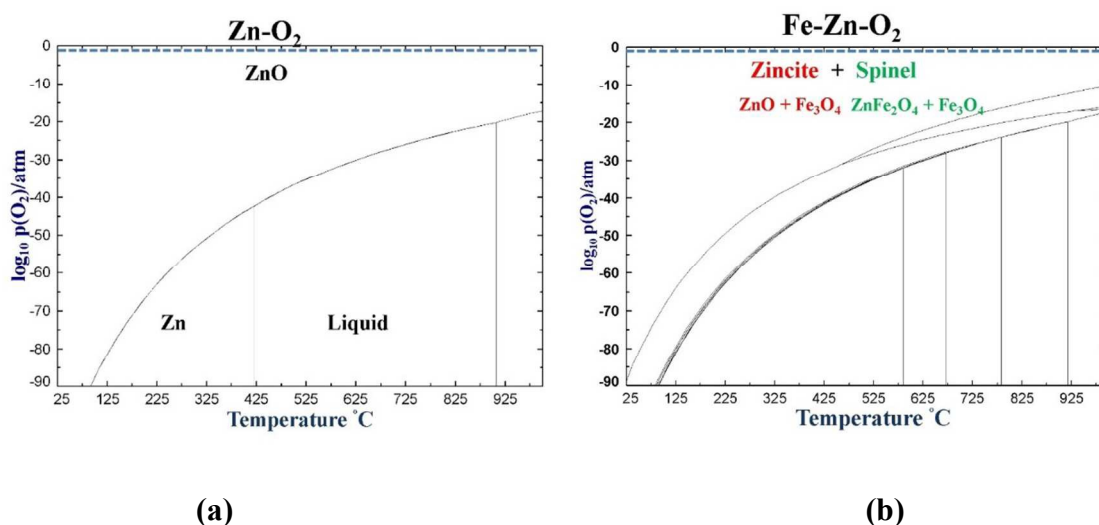
Fig 14. (a) Binary phase diagram of Zn-O system (b) Ternary phase diagram of Fe-Zn-O system.

The experimental data (EDS and Raman) on the chemical nature of the mixed oxides were further corroborated by thermodynamic calculations. The calculations were performed through thermodynamic software Factsage[34] using FToxide databases. As seen in Fig. 14 (a)-(b) ZnO phase is expected at 25 °C and atmospheric oxygen concentration in case of pure Zn, whereas a mixture of Zincite ($ZnO + Fe_3O_4$) and Spinel ($ZnFe_2O_4 + Fe_3O_4$) is possible in Fe-Zn-O system under the same conditions (at 25 °C and atmospheric oxygen concentration).

The schematic depicting the sequence of the wear process for both Zn $_{(100)}$ and Zn $_{(002)}$ coatings are shown in Fig. 14. For $Zn_{(100)}$ three different stages were identified: (1) Transfer film formation and strain hardening, (2) transfer film removal from the ball surface and oxidation of the counter surface (3) formation of iron oxide and zinc oxide mixture followed by steady state friction. For $Zn_{(002)}$, sequence of the wear process are: (1) Steady material removal with some transfer film at the early stage (2) direct contact of steel ball-steel substrate resulting in iron oxide on both ball and track surface, (3) Oxidation of the Zn debris followed by steady state friction.
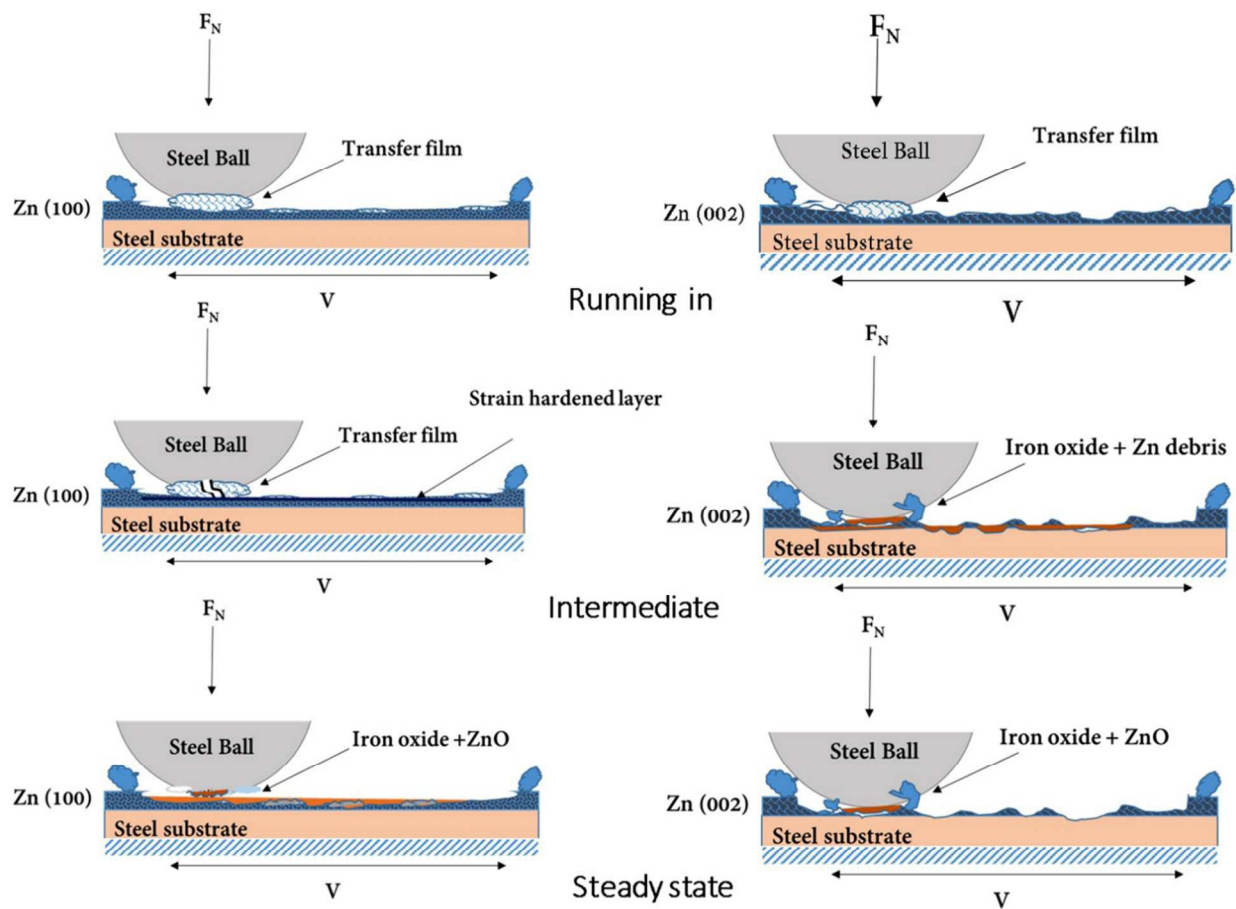
Fig 15. Schematic illustrating the wear behaviour of Zn $_{(100)}$ and Zn $_{(002)}$ coatings

Even though both the coatings showed the presence of lubricious oxides, they originated from two different scenarios. For Zn $_{(100)}$ system, most of the coating was intact throughout the test and iron oxide peak first detected on ball surface (figure 12b, 200 cycles). A thicker black oxide debris was observed on the ball surface at 500 cycles (see figure 12c, 500 cycles). Above 500 cycles, the granular oxide debris entered the sliding contact and smearing of oxide debris resulted in a friction rise (figure 5a, cycle 500 to 750). Once a smooth transfer film is formed on ball surface, friction started to stabilize. The optical micrograph of the ball surface at 850 and

1200 cycles showed smooth patches of iron oxide covering majority of the contact area. The sliding of oxide transfer film (on ball surface) against the iron oxide and zinc oxide patches on the wear track resulted in steady state friction. For Zn $_{(002)}$ coating, prior to steady state friction most of the coating was consumed by the wear process and direct rubbing of steel ball against steel substrate produced iron oxide and redeposited oxide films dominated the steady state friction regime.

Both Zn $_{(100)}$ and Zn $_{(002)}$ showed similar steady state friction. However, at the end of wear test most of the Zn $_{(002)}$ coating was consumed and the steady state friction came from lubricious oxide films[27] not from the original coating. On the other hand, Zn $_{(100)}$ coating showed superior wear characteristics. For Zn protective coatings, it is not the low shear strength rather higher hardness and naturally formed ZnO determines the wear characteristics.

Conclusions

The tribological behaviour of coatings with different preferred orientations was observed to be different. The initial peak friction and the run in behaviours were observed to be higher in Zn $_{(100)}$ coating than the Zn $_{(002)}$ coating. Both the coatings showed formation of transfer films during run in behaviour. The steady state friction after the run in behaviour was also observed to be same except the Zn $_{(100)}$ coating showed some instability. The wear rate of the Zn $_{(100)}$ coating was lower than the Zn $_{(002)}$ coating. Mixed mode oxidation was observed in the steady state friction regime for both the coatings, but the onset of iron oxide formation was earlier in Zn $_{(002)}$ coating. From tribological application point of view, harder Zn $_{(100)}$ coatings with naturally formed or reactively formed ZnO layers are preferred than softer basal slip dominant Zn $_{(002)}$ coatings.

Acknowledgement

References

1.   R. Winand, in *Modern Electroplating*, John Wiley & Sons, Inc., 2010, DOI: 10.1002/9780470602638.ch10, pp. 285-307.
2.   I. Tomov, C. Cvetkova, V. Velinov, A. Riesenkampf and B. Pawlik, *Journal of Applied Electrochemistry*, 1989, **19**, 377-382.
3.   M. Mouanga, L. Ricq, G. Douglade, J. Douglade and P. Berçot, *Surface and Coatings Technology*, 2006, **201**, 762-767.
4.   M. Mouanga, L. Ricq, J. Douglade and P. Berçot, *Journal of Applied Electrochemistry*, 2007, **37**, 283-289.
5.   K. Raeissi, M. R. Bateni, A. Saatchi, M. A. Golozar and J. A. Szpunar, *Surface and Coatings Technology*, 2006, **201**, 3116-3122.
6.   K. Raeissi, A. Saatchi and M. A. Golozar, *Journal of Applied Electrochemistry*, 2003, **33**, 635-642.
7.   K. Raeissi, A. Saatchi, M. A. Golozar and J. A. Szpunar, *Journal of Applied Electrochemistry*, 2004, **34**, 1249-1258.
8.   K. Raeissi, A. Saatchi, M. A. Golozar and J. A. Szpunar, *Surface and Coatings Technology*, 2005, **197**, 229-237.
9.   ASTM-F1941-00, *Journal*, DOI: 10.1520/F1941-07
10.   K. R. Sriraman, H. W. Strauss, S. Brahimi, R. R. Chromik, J. A. Szpunar, J. H. Osborne and S. Yue, *Tribology International*, 2012, **56**, 107-120.
11.   K. R. Sriraman, S. Brahimi, J. A. Szpunar, J. H. Osborne and S. Yue, *Electrochimica Acta*, 2013, **105**, 314-323.
12.   K. R. Sriraman, S. Brahimi, J. A. Szpunar and S. Yue, *Journal of Applied Electrochemistry*, 2013, **43**, 441-451.
13.   Q. Li, Z. Feng, J. Zhang, P. Yang, F. Li and M. An, *RSC Advances*, 2014, **4**, 52562-52570.
14.   Q. Li, Z. Feng, L. Liu, H. Xu, W. Ge, F. Li and M. An, *RSC Advances*, 2015, **5**, 32479-32490.
15.   Q. Li, Z. Feng, L. Liu, J. Sun, Y. Qu, F. Li and M. An, *RSC Advances*, 2015, **5**, 12025-12033.
16.   J. Giridhar and W. J. van Ooij, *Surface and Coatings Technology*, 1992, **53**, 35-47.
17.   A. C. Hegde, K. Venkatakrishna and N. Eliaz, *Surface and Coatings Technology*, 2010, **205**, 2031-2041.
18.   H. W. Strauss, R. R. Chromik, S. Hassani and J. E. Klemberg-Sapieha, *Wear*, 2011, **272**, 133-148.
19.   R. R. Chromik, H. W. Strauss and T. W. Scharf, *JOM*, 2012, **64**, 35-43.

20. K. J. Wahl and I. L. Singer, *Tribol Lett*, 1995, **1**, 59-66.
21. W. C. Oliver and G. M. Pharr, *Journal of Materials Research*, 1992, **7**, 1564-1583.
22. G. M. Pharr and W. C. Oliver, *MRS Bulletin*, 1992, **17**, 28-33.
23. L. E. Morón, A. Méndez, F. Castañeda, J. G. Flores, L. Ortiz-Frade, Y. Meas and G. Trejo, *Surface and Coatings Technology*, 2011, **205**, 4985-4992.
24. R. Parisot, S. Forest, A. Pineau, F. Grillon, X. Demonet and J.-M. Mataigne, *Metallurgical and Materials Transactions A*, 2004, **35**, 797-811.
25. C. N. Panagopoulos, K. G. Georgarakis and S. Petroutzakou, *Journal of Materials Processing Technology*, 2005, **160**, 234-244.
26. A. Nazeer, PhD, California Institute of Technology, PhD thesis, 1965.
27. J. S. Zabinski, J. Corneille, S. V. Prasad, N. T. Mc Devitt and J. B. Bultman, *Journal of Materials Science*, 1997, **32**, 5313-5319.
28. K. A. Alim, V. A. Fonoberov, M. Shamsa and A. A. Balandin, *Journal of Applied Physics*, 2005, **97**, 124313.
29. Q. Tian, Q. Wang, Q. Xie and J. Li, *Nanoscale Research Letters*, 2010, **5**, 1518 - 1523.
30. I. G. Aksyanov, M. E. Kompan, I. V. Kul'kova and Y. P. Stepanov, *Glass Physics and Chemistry*, 2012, **38**, 143-148.
31. S. Oh, D. C. Cook and H. E. Townsend, *Hyperfine Interactions*, 1998, **112**, 59-66.
32. S.-H. Shim and T. S. Duffy, *American Mineralogist*, 2002, **87**, 318-326.
33. O. N. Shebanova and P. Lazor, *Journal of Raman Spectroscopy*, 2003, **34**, 845-852.
34. C. W. Bale, E. Bélisle, P. Chartrand, S. A. Decterov, G. Eriksson, K. Hack, I. H. Jung, Y. B. Kang, J. Melançon, A. D. Pelton, C. Robelin and S. Petersen, *Calphad*, 2009, **33**, 295-311.

240x180mm (150 x 150 DPI)